Science Bulletin xxx (xxxx) xxx

Contents lists available at ScienceDirect

Science Bulletin

journal homepage: www.elsevier.com/locate/scib

Article

Sulfur atom-directed metal–ligand synergistic catalysis in zirconium/hafnium-oxo clusters for highly efficient amine oxidation

Sheng-Nan Sun [a,1], Qian Niu [c,1], Jiao-Min Lin [a,*], Li-Ling He [a], Jing-Wen Shi [a], Qing Huang [b], Jiang Liu [a,*], Ya-Qian Lan [a,*]

[a] School of Chemistry, South China Normal University, Guangzhou 510006, China
[b] College of Materials Science and Engineering, Nanjing Forestry University, Nanjing 210037, China
[c] School of Chemistry and Materials Science, Nanjing Normal University, Nanjing 210023, China

ARTICLE INFO

Article history:
Received 8 September 2023
Received in revised form 23 October 2023
Accepted 17 November 2023
Available online xxxx

Keywords:
Zirconium/Hafnium-oxo clusters
Amine oxidation reaction
Photocatalytic reaction
Synergistic catalysis

ABSTRACT

The performance applications (e.g., photocatalysis) of zirconium (Zr) and hafnium (Hf) based complexes are greatly hindered by the limited development of their structures and the relatively inert metal reactivity. In this work, we constructed two ultrastable Zr/Hf-based clusters (Zr_9-TC4A and Hf_9-TC4A) using hydrophobic 4-*tert*-butylthiacalix[4]arene (H_4TC4A) ligands, in which unsaturated coordinated sulfur (S) atoms on the $TC4A^{4-}$ ligand can generate strong metal–ligand synergy with nearby active metal Zr/Hf sites. As a result, these two functionalized H_4TC4A ligands modified Zr/Hf-oxo clusters, as catalysts for the amine oxidation reaction, exhibited excellent catalytic activity, achieving very high substrate conversion (>99%) and product selectivity (>90%). Combining comparative experiments and theoretical calculations, we found that these Zr/Hf-based cluster catalysts accomplish efficient amine oxidation reactions through synergistic effect between metals and ligands: (i) the photocatalytic benzylamine (BA) oxidation reaction was achieved by the synergistic effect of the dual active sites, in which, the naked S sites on the $TC4A^{4-}$ ligand oxidize the BA by photogenerated hole and oxygen molecules are reduced by photogenerated electrons on the metal active sites; (ii) in the aniline oxidation reaction, aniline was adsorbed by the bare S sites on ligands to be closer to metal active sites and then oxidized by the oxygen-containing radicals activated by the metal sites, thus completing the catalytic reaction under the synergistic catalytic effect of the proximity metal–ligand. In this work, the Zr/Hf-based complexes applied in the oxidation of organic amines have been realized using active S atom-directed metal–ligand synergistic catalysis and have demonstrated very high reactivity.

1. Introduction

The elements of group IVB (titanium (Ti), zirconium (Zr), and hafnium (Hf)) have been widely used in the fields of atomic energy, aerospace, and medical devices due to their hardness, corrosion resistance, and high thermal conductivity [1–4]. Among them, for applications in the field of catalysis, the elements of this group are mainly concentrated in their oxides [5]. However, oxides not only inherently have little structural variation, but also mainly utilize the intrinsic activity of metals for catalytic reactions, thus greatly limiting the improvement of catalytic performance and the expansion of catalytic reaction types. Considering the strong Lewis acidity and high coordination number of the elements in group IVB, the design and synthesis of their corresponding complexes are considered as an important way to expand the structural diversity and catalytic reaction types [6–8]. Through the modification of functionalized ligands, the group IVB metal-containing complex catalysts not only exhibit flexible structural compositions but also enable effective modulation of catalytic reaction types and performance [9–11]. Nevertheless, the hydrolytic nature of metals in this group makes the crystallization of their complexes very difficult [12,13], and therefore the development of the structures and catalytic applications of the group IVB metal-containing complexes are still very limited. Moreover, most catalytic applications, especially photocatalysis, of the existing complex catalysts of this group are concentrated on Ti, while the development of Zr and Hf is rare [14–18], because the large atomic radius of Zr and Hf leads to their low reaction activity, and their strong binding ability with oxygen

* Corresponding authors.
E-mail addresses: linjm@m.scnu.edu.cn (J.-M. Lin), liuj0828@m.scnu.edu.cn (J. Liu), yqlan@m.scnu.edu.cn (Y.-Q. Lan).
[1] These authors contributed equally to this work.

https://doi.org/10.1016/j.scib.2023.11.047
2095-9273/

makes their complex structural units immobilized, thus limiting the diversity of structures [6].

To effectively develop the catalytic applications (e.g., photocatalysis) of Zr/Hf-based complexes and improve their corresponding performance, most of the current researches have been devoted to the construction of Zr/Hf-based metal–organic frameworks (MOFs), which are composed of functional ligands and limited Zr/Hf-oxo clusters (usually with a nucleus number ≤6) [19–25]. Compared to MOFs, constructing Zr/Hf-based clusters seems to have greater catalytic potential. This is because they not only have the same ligand-regulated advantages of MOFs but also have a lower dimensionality, which allows the substrate to be more accessible to the active sites [26–30]. Furthermore, more metal active sites can be exposed by further increasing the nuclearity [31–33]. At present, the main strategy to improve the catalytic performance of Zr/Hf-based clusters is to regulate the electronic structure and coordination environment of metal active sites by modifying them with functional ligands [34–36]. However, we believe that it may be a more effective strategy to further enhance the catalytic performance, if functional ligands can be used together with metal active sites to catalyze specific reactions (Fig. 1). Moreover, to successfully implement this synergistic strategy, we speculate that in the catalyst structure, a reasonable spatial distribution and adjacent spatial distance between the Zr/Hf active site and the functional ligand are also required.

To explore the reliability of the above strategy in modulating the performance of Zr/Hf-based complex catalysts, we synthesized two ultrastable Zr/Hf-based clusters functionalized by *p-tert*-butylthiacalix[4]arene (**H_4TC4A**) (Zr_9(TC4A)$_3$(μ_3-O)$_4$(μ_4-O)$_3$(μ_3-OH)(HCOO)$_3$(OH)$_3$(CH_3O)$_3$(DMF)$_3$ (**Zr_9-TC4A**), and Hf_9(TC4A)$_3$(μ_3-O)$_4$(μ_4-O)$_3$(μ_3-OH)(HCOO)$_3$(OH)$_3$(CH_3O)$_3$(DMF)$_3$ (**Hf_9-TC4A**)). **H_4TC4A** is a bowl-shaped macrocyclic ligand containing four phenolic units and linked by four sulfur (S) atoms, and its unique molecular crystallographic conformation usually leads to an adjacent spatial distribution and distance between the soft base S atom and the hard acidic metal (e.g., Zr, Hf) active site [37–42]. In this case, the S atom can be a potential non-metallic catalytic active site that synergizes with the metal active site. As expected, both **Zr_9-TC4A** and **Hf_9-TC4A** exhibit very high substrate conversion (>99%) and product selectivity (>90%) when they were used as catalysts for photocatalytic oxidative coupling reaction of benzylamine and aniline oxidation reactions under hydrogen peroxide system. Experiments and theoretical calculations show that unsaturated S atom on **TC4A^{4-}** has an important role in the reaction: (i) in the benzylamine oxidation reaction, under irradiation, photogenerated electron holes are enriched in S sites to activate benzylamine molecule, and then co-operate with metal active sites to complete the catalytic reaction; (ii) in the oxidation of aniline, active S site can adsorb and lock the aniline substrate due to the strong adsorption and thus close the distance to the metal reactive site to complete the catalytic reaction together. This work effectively improves the catalytic performance of Zr/Hf-based clusters and expands their applications in catalytic organic oxidation reactions by establishing unsaturated S atom-directed ligand engineering, which provides an important feasibility strategy for designing high-performance Zr/Hf-based complex catalysts and developing more catalytic reaction types in the future.

2. Materials and methods

2.1. Synthesis of *Hf$_9$-TC4A* and *Zr$_9$-TC4A*

*Synthesis of **Hf$_9$-TC4A***. $HfCl_4$ (16.00 mg, 0.05 mmol) and H_4TC4A (7.20 mg, 0.01 mmol) were dissolved in a mixed solution (*N*,*N*-dimethylformamide:methanol = 2:1, v/v), then the mixture was transferred to a 10 mL scintillation vial. The vial was put in an oven and heated at 100 °C for 72 h. After cooling down to room temperature, colorless square crystals were obtained.

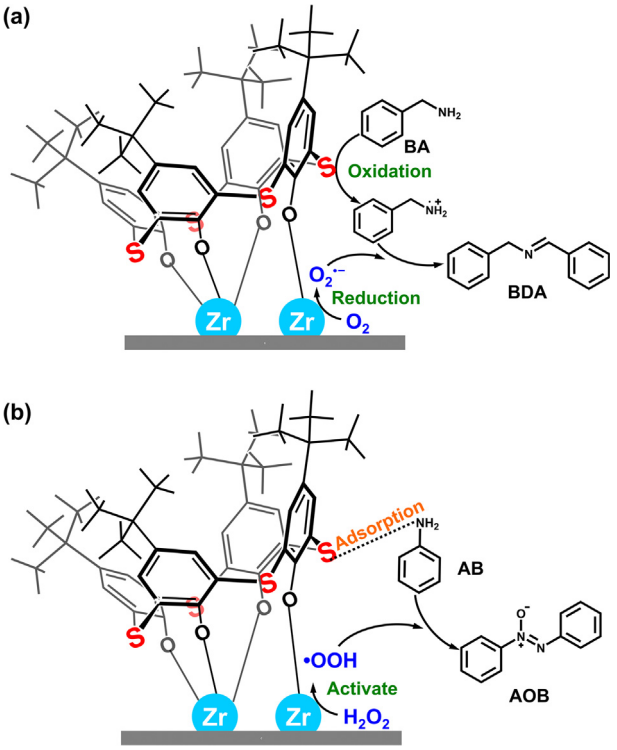

Fig. 1. (Color online) Two possible synergistic strategies. (a) Two active sites; (b) one adsorption site and one active site.

*Synthesis of **Zr$_9$-TC4A***. The synthesis process is similar to the above process, except that $HfCl_4$ was instead of $ZrCl_4$ (12.00 mg, 0.04 mmol). After cooling down to room temperature, colorless square crystals were obtained.

2.2. Characterization

Powder X-ray diffraction (PXRD) spectra of the samples were recorded on a Rigaku SmartLab diffractometer (Japan) equipped with Cu Kα (λ = 1.54060 Å) radiation at 40 kV and 200 mA. Fourier transform infrared spectroscopy (FTIR) was recorded on a Nicolet iS50 Fourier transform infrared spectrometer (Thermo Scientific, USA) in the range of 4000–400 cm^{-1} using the technique of pressed KBr pellets. Thermogravimetric analysis (TGA) was carried out on a STA449F3 analyzer (Netzsch, Germany) under the oxygen atmosphere heated from room temperature to 800 °C. UV–visible (UV–Vis) absorption spectra were acquired on a Cary 5000 (Varian, USA) in the wavelength range of 250–800 nm. Electron paramagnetic resonance (EPR) experiments were conducted on EMX PLUS (Bruker, Germany). The electrochemical tests were carried out with an EC-Lab SP-150 workstation (Bio-Logic, France). ^{1}H nuclear magnetic resonance (NMR) and ^{13}C NMR were carried out by AVANCE III 400 M spectrometer (Bruker, Germany). Chemical shifts (δ) are reported in parts per million (ppm) relative to incompletely deuterated $CDCl_3$ (s, 7.26 ppm). The catalytic liquid products were analyzed by gas chromatography-mass spectrometer (GC-MS) (Agilent 7890B and 5977B equipped HP-5-MSUI or HP-PLOT Molesieve capillary column, USA). Single-crystal XRD data of crystals were measured on an APEXII CCD diffractometer (Bruker, Germany) with graphite-monochromated Mo Kα radiation (λ = 0.71073 Å) at 296 K. All the structures were solved by direct method using SHELXT program and refined on an Olex2 software.

The detailed crystallographic information of these crystals is listed in Table S1 (online). The Cambridge Crystallographic Data Centre (CCDC) numbers of **Hf_9-TC4A** and **Zr_9-TC4A** are 2252126 and 2252190.

2.3. Photocatalytic oxidative coupling of benzylamines

Typically, the photocatalyst (5 mg) was dispersed in 2 mL of CH_3CN containing 0.1 mmol benzylamines (BA) in a quartz reactor (10 mL) and the photoreactor was sealed. A 300 W Xenon lamp (light intensity: 200 mW cm^{-2}, Beijing China Education Au-Light Co., Ltd., China) with a full spectrum was used as a light source. The reaction temperature was controlled at 298 K by using the cooling water circulation. After the reaction, the solution was collected, centrifuged, and filtered through a 0.22 μm syringe filter to remove the solid catalyst. The filtrate was identified by GC-MS, and the conversion and selectivity were analyzed by GC. Other benzylamine derivatives with the same concentration were conducted using a similar approach and the corresponding conversion was analyzed by NMR spectroscopy.

The conversion of BA and selectivity for *N*-benzylidenebenzylamine (BDA) product, were calculated with the following Eqs. (1) and (2):

$$\text{Conversion}\ (\%) = \frac{C_0 - C_{BA}}{C_0} \times 100, \quad (1)$$

$$\text{Selectivity}\ (\%) = \frac{2\ C_{BDA}}{C_0 - C_{BA}} \times 100, \quad (2)$$

where C_0 is the initial concentration of BA; C_{BA} and C_{BDA} stand for the concentration of the residual BA and the corresponding product of BDA at a certain time after the catalytic reaction, respectively.

2.4. Photoelectrochemical measurements

Preparation of the working electrode: 2 mg photocatalysts were mixed with 990 μL ethanol and 10 μL Nafion D-520 dispersion solutions with sonicating for 30 min. Subsequently, 200 μL of slurry was transferred and coated on an indium-tin-oxide (ITO) glass plate (1 cm × 2 cm) and then dried at room temperature.

Photocurrent response measurements were carried out on a CHI 660E electrochemical workstation in a standard three-electrode electrochemical cell with the catalyst-modified ITO glass plate as the working electrode, platinum plate as a counter electrode, and an Ag/AgCl electrode (with saturated KCl) as a reference electrode. A sodium sulfate solution (Na_2SO_4, 0.2 mol L^{-1}) was used as the electrolyte. A xenon lamp with full spectrum as the light source.

Mott-Schottky plots were conducted in the electrochemical workstation (Bio-Logic, France) via a conventional three-electrode system with a working electrode, a platinum plate as a counter electrode, and a Ag/AgCl electrode as a reference electrode in 0.2 mol L^{-1} Na_2SO_4 aqueous solution (pH 6.8) at different frequencies of 500, 1000, and 1500 Hz. The preparation of the working electrode was the same as that of photocurrent response measurements.

Electrochemical impedance spectra (EIS) measurements were also carried out on the electrochemical workstation (Bio-Logic, France) via a conventional three-electrode system in 0.2 mol L^{-1} Na_2SO_4 aqueous solution over a frequency range of 100 kHz–0.1 Hz.

The EPR spectra were obtained in the presence of 5,5-dimethyl-1-pyrroline-N-oxide (DMPO). Typically, 5 μL DMPO was mixed with 0.5 mL of photocatalyst/CH_3CN suspension (2 mg/0.5 mL). The formed mixture (50–100 μL) was added into the EPR tube. EPR measurements were carried out during the light irradiation with a 300 W Xenon lamp under air conditions.

2.5. General procedure for aniline oxidation

The mixture of aniline, catalyst, and methanol is transferred to a glass bottle in the air. Then, a certain amount of H_2O_2 (30%, w/w) was added to the reaction vessel. The mixture was stirred at room temperature for a certain time. After the reaction, the filtrate is collected by filtering. The products were determined by GC-MS and quantified by GC. The resulting reaction products of aniline derivatives were characterized by NMR spectroscopy. The calculation of the conversion of substrate and the selectivity of products are the same as those of the benzylamine oxidation process.

2.6. In-situ FTIR measurement

The *in-situ* FTIR spectra of benzylamine (BA) adsorbed on samples were carried out on a Nicolet iS50 Fourier transform infrared (FT-IR) spectrometer (Thermo Scientific, USA). Firstly, a powder sample (catalysts mixed with KBr) was pressed into a self-supporting sample cell. Before measurements, the sample cell was treated under a N_2 atmosphere at 120 °C for 1 h to remove surface contaminants. After the sample cell cooling to room temperature, 5 μL of benzylamine was spiked into the cell with a syringe. After adsorption equilibrium was reached 30 min later, turning on the 300 W Xe lamp and infrared spectra were recorded from 0 to 60 min.

3. Results and discussion

3.1. Structure and characterization of clusters

The colorless Zr/Hf-based clusters modified by **H_4TC4A** were both successfully synthesized via solvent thermal reaction (Figs. S1, S2 online). Single-crystal X-ray diffraction analysis reveals that **Hf_9-TC4A** and **Zr_9-TC4A** are isomorphic. **Zr_9-TC4A** was taken as an example to introduce their structure in detail. **Zr_9-TC4A** crystallizes in the cubic *I*-43*m* space group and each molecule contains nine Zr atoms, three calixarenes ligands, and three *N*,*N*-dimethylformamide (DMF) molecules (Fig. S3 online). The nine Zr atoms are connected by six μ_2-O, eight μ_3-O, and three μ_4-O to form the Zr_9-oxo core (Fig. 2). As shown in Fig. 2c, except for the six-coordinated Zr3 atoms, Zr1 and Zr2 atoms are both seven-coordinated. Especially, each Zr1 atom is coordinated with one DMF molecule. The overall metal-oxo core is firmly anchored in the cavity of three **$TC4A^{4-}$** ligands, in which each **$TC4A^{4-}$** uses three O atoms (two O6 and one O2) to coordinate with Zr3 atom, and one O atom (O7) to coordinate with Zr2 atom. Noteworthily, the S atoms on the **$TC4A^{4-}$** ligand are exposed, which do not coordinate with any additional atoms and the distances between S and Zr are in the range of 3.96 to 7.52 Å (Table S1 online). Compared to **Hf_9-TC4A** and **Zr_9-TC4A**, though **Hf_9-SO_4** and **Zr_9-SO_4** have similar metal-oxo cores to **Hf_9-TC4A** and **Zr_9-TC4A**, their periphery is both coordinated by fourteen SO_4^{2-} with four-coordinated S atoms (Fig. 2).

The phase purity of the prepared complexes **Hf_9-TC4A**, **Zr_9-TC4A**, **Hf_9-SO_4**, and **Zr_9-SO_4** was determined by PXRD (Figs. S4–S7 online). The *p*-*tert*-butyl groups of calixarene in complexes **Hf_9-TC4A** and **Zr_9-TC4A** were characterized by FTIR spectra (Figs. S8–S11 online), in which, the peak at 2965 cm^{-1} can be ascribed to C–H vibration bands of **H_4TC4A**. Moreover, the chemical stability of **Hf_9-TC4A** and **Zr_9-TC4A** was evaluated by immersing samples in aqueous solutions with different pH values. As shown in Figs. S12 and S13 (online), the PXRD peaks that match well with the simulated peaks indicate the good stability of the **Hf_9-TC4A** and **Zr_9-TC4A**. In addition, the thermal stabilities of these complexes were confirmed by thermogravimetric analysis

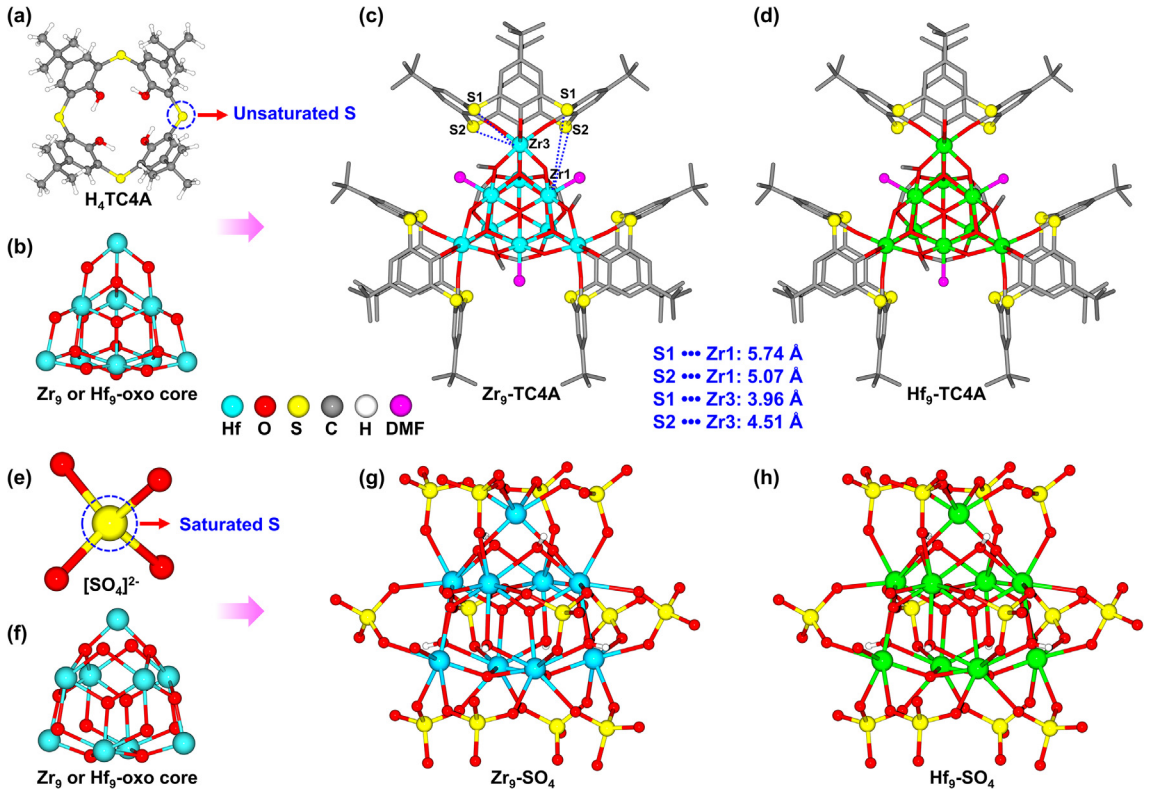

Fig. 2. (Color online) Simplify of the structures of **Zr_9-TC4A** and **Zr_9-SO_4**.

(Figs. S14–S17 online) and all frameworks are stable up to at least ca. 400 °C in air. These results suggest that **Hf_9-TC4A** and **Zr_9-TC4A** have good stability, which provides a good foundation for their further performance applications.

3.2. Catalytic performance

Subsequently, the photophysical properties of **Hf_9-TC4A** and **Zr_9-TC4A** were investigated due to the special structural characteristics of calixarene and their applications in the field of photocatalysis [43–45]. The UV–Vis diffuse reflectance spectroscopy was recorded. As shown in Fig. 3a, both **Zr_9-TC4A** and **Hf_9-TC4A** exhibited a similar light absorption range with an edge around 380 nm. Based on the UV–Vis spectra, the optical band gaps (E_g) of **Zr_9-TC4A** and **Hf_9-TC4A** were calculated by the Kubelka–Munk (KM) method from the Tauc plots, which are about 3.54 and 3.57 eV, respectively (Fig. 3b). Significantly, compared with **Zr_9-SO_4** and **Hf_9-SO_4**, it is obvious that **Zr_9-TC4A** and **Hf_9-TC4A** display a greatly enhanced light absorption, which may be ascribed to the modification of calixarene that changes the electronic structures of the clusters (Fig. 3a). Then, Mott–Schottky electrochemical measurements were conducted together to evaluate the band structures of photocatalysts and explore the lowest unoccupied molecular orbital (LUMO) positions of photocatalysts. As presented in Fig. 3c and Figs. S18, S19 (online), the Mott–Schottky plot of **Zr_9-TC4A** and **Hf_9-TC4A** have positive slopes, revealing an n-type semiconductor behavior. Thus, their flat band potential (E_{fb}) is −1.30 and −1.40 V vs. Ag/AgCl, respectively, and the LUMO value of **Zr_9-TC4A** and **Hf_9-TC4A** were estimated to be −1.10 and −1.20 V vs. normal hydrogen electrode (NHE), respectively, due to the bottom of LUMO nearly equals to the E_{fb} in the n-type semiconductors. Subsequently, according to the value of E_g and LUMO, the corresponding highest occupied molecular orbital (HOMO) positions of **Zr_9-TC4A** and **Hf_9-TC4A** were further ascertained to be 2.44 and 2.37 V vs. NHE, respectively. Obviously, these photocatalysts have a much positive HOMO value, which allows them a potential application in various photoinduced organic synthesis reactions such as amine oxidation (Fig. 3c). Besides, the transient photocurrent response measurements and EIS experiments were carried out to evaluate the charge-separation efficiency of photocatalysts, which is an important influencing factor for photocatalytic processes. As displayed in Fig. S20 (online), **Zr_9-TC4A** and **Hf_9-TC4A** have stronger intensities of the transient photocurrent responses than that of **Zr_9-SO_4** and **Hf_9-SO_4**, suggesting a better photoinduced charges transfer. Moreover, the EIS for **Zr_9-TC4A** and **Hf_9-TC4A** show a smaller radius in comparison with **Hf_9-SO_4** and **Zr_9-SO_4**, indicating lower charge-transfer resistance that can achieve higher efficiency for charge transfers (Figs. S21, S22 online). These results prove that **Zr_9-TC4A** and **Hf_9-TC4A** can be potential photocatalysts.

The appropriate band structure is one of the most important parameters of catalysts for photocatalytic reactions. It can be seen that these LUMO values are more negative than the theoretical potential for the reduction of O_2 to superoxide radical (−0.33 V vs. NHE) [46,47], a key active species in organic oxidation reactions, which suggests that the **Zr_9-TC4A** and **Hf_9-TC4A** are theoretically feasible for the photocatalytic conversion of O_2 to superoxide radical anions (O_2^{-}) intermediate (Fig. 3c). Given the excellent photophysical properties mentioned above, the photocatalytic oxidative coupling reaction of BA was performed, which involves molecular oxygen activation and organic coupling reaction. After systematic optimization, when **Zr_9-TC4A** (or **Hf_9-TC4A**, 5 mg) and benzylamine (0.1 mmol) in 2 mL of CH_3CN was irradiated over a 300 W Xenon lamp (light intensity: 200 mW cm^{-2}) with a full spectrum under air at room temperature, the formation of BDA with a considerable conversion (99% and 97.4%, Fig. 3d and Figs. S23, S24 online) was observed. Then, a series of control experiments were conducted to determine the indispensable reaction conditions. As demonstrated in Table S3 (entries 2–4, online), the

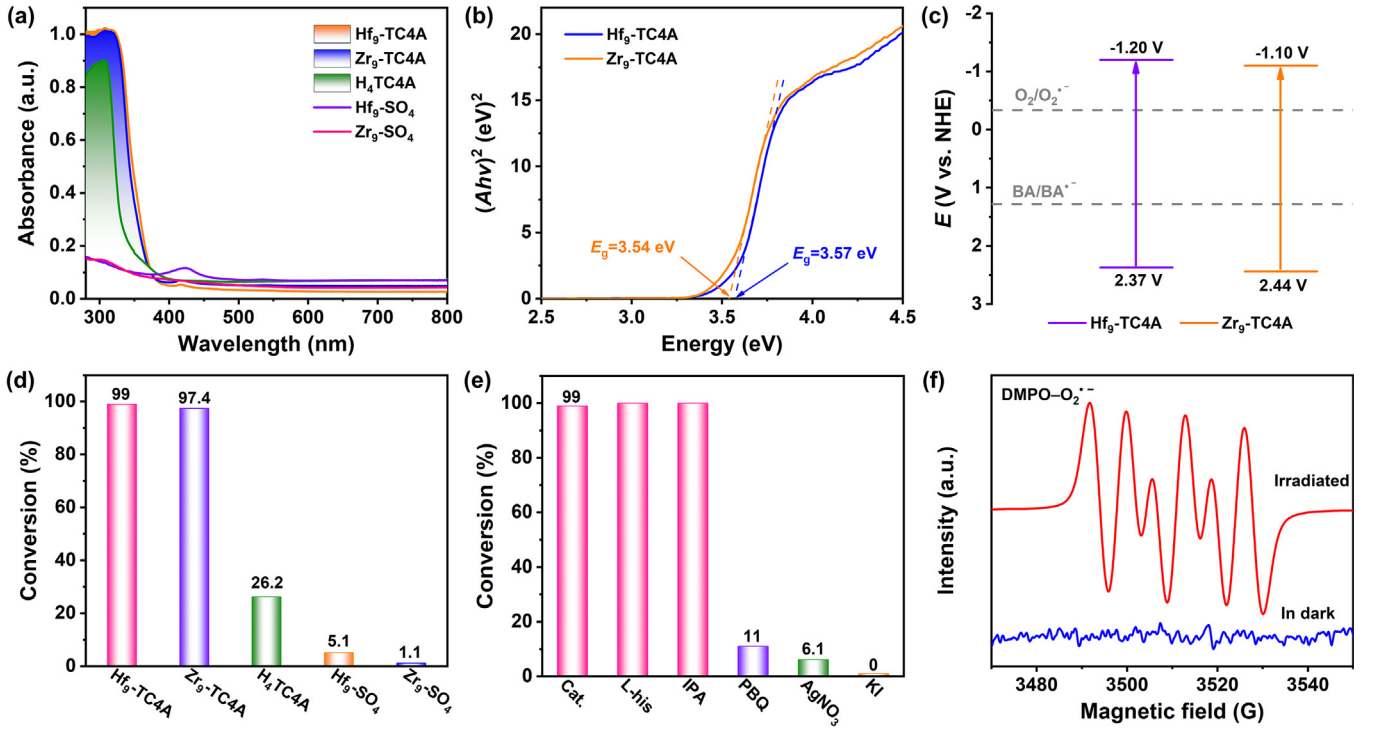

Fig. 3. (Color online) The photophysical properties of samples and the performance of photocatalytic oxidative coupling reaction of benzylamines. (a) The UV–Vis diffuse reflection spectra for samples. (b) Tauc plots of **Zr_9-TC4A** and **Hf_9-TC4A**. *A* is the absorption coefficient and $h\nu$ is the photon energy. (c) Energy band diagrams of two clusters. (d) Conversion of oxidative coupling of benzylamine. (e) Some comparative tests with the corresponding sacrificial reagents. (f) EPR spectra of **Hf_9-TC4A** under irradiated and in the dark in the presence of DMPO.

photocatalyst, oxygen, and light are all essential conditions for the oxidative amine coupling reaction of BA, otherwise, only a little or trace conversion can be observed. To investigate the origin of the good performance, the activities of **Hf_9-SO_4** and **Zr_9-SO_4** for oxidative amine coupling reaction of BA were evaluated and the results show that their performance is very poor with an extremely low conversion of 5.1% and 1.1%, respectively (Fig. 3d). Such a large performance difference may be origin from the modification of calixarene on the **Hf_9-TC4A** and **Zr_9-TC4A**. Besides, another comparative experiment was conducted to measure the performance of the physical mixture (**H_4TC4A** and metal salts). As displayed in Fig. S25 (online), the physical mixture shows very poor catalytic performance with a conversion of less than 25%, which demonstrates the advantages of binding between ligands and metals in the reaction.

To explore the mechanism of the photocatalytic reaction, a series of quenching experiments were performed to determine the key intermediates in the photocatalytic transformation (Table S3, entries 5–9 online) [48]. The addition of L-histidine and *iso*-propanol (IPA) shows a negligible decrease in the reaction conversion, which rules out the existence of $^1O_2$ and ·OH radicals during photocatalysis. Then, *p*-benzoquinone (PBQ), $AgNO_3$, and KI are used as $O_2^{\cdot-}$, photogenerated electron, and hole scavenger, respectively, to be added to the mixture reaction. The significantly decreasing conversion of BA indicates that $O_2^{\cdot-}$ radical, photogenerated electron, and hole are very important to the amine coupling reaction. Furthermore, electron paramagnetic resonance (EPR) experiments with DMPO as a capture agent were carried out to further measure the active species. As presented in Fig. 3f, for **Hf_9-TC4A** and **Zr_9-TC4A**, almost no signals of $O_2^{\cdot-}$ were captured in the dark. However, the characteristic $O_2^{\cdot-}$ EPR signal intensity for **Hf_9-TC4A** and **Zr_9-TC4A** is significantly enhanced under visible light irradiation, which confirms the generation of $O_2^{\cdot-}$ radical in the photocatalytic reaction and suggests that photogenerated electrons might facilitate the reduction of O_2 to form $O_2^{\cdot-}$. By contrast, the characteristic $O_2^{\cdot-}$ EPR signal intensity for **Hf_9-SO_4** and **Zr_9-SO_4** is so weak (Fig. S26 online), which shows the importance of the modified **H_4TC4A** in photocatalytic reactions.

To in-depth understand the reaction process of BA photo-conversion to BDA, the *in-situ* diffuse reflectance infrared Fourier transform spectroscopy (DRIFTS) measurement was performed (Fig. 4) [49,50]. In the dark, after achieving the adsorption equilibrium for 20 min, no new IR band/peak is observed at 0 min, suggesting the photocatalytic nature of BA photo-conversion to BDA. With the stimulation of light, new IR peaks at 1643 and 2897 cm^{-1} appear, which can be assigned to the C=N and C–H stretching vibrations of the benzyl imine intermediate, respectively. As time goes on, the product BDA generates, as suggested by the appearance of the C=N stretching vibration (1652 cm^{-1}) for BDA. This phenomenon indicates that the product BDA can form via the pathway that benzyl imine intermediate nucleophilic attacked by BA molecules. Meanwhile, the peaks at 1604 and 3309 cm^{-1} of N–H bending and stretching vibrations grow up, which indicates the formation of NH_3 with the production of BDA. In addition, we also observe the characteristic IR peak of the C=O bond appears at 1700 cm^{-1}, which indicates that there is another pathway involved benzaldehyde intermediate for the BA photo-conversion to BDA in our photocatalytic system.

Moreover, the density functional theory (DFT) calculations were performed to further investigate the underlying cause of the clusters' high activity. Fig. 5a displays the HOMO and LUMO orbitals of **Hf_9-TC4A**, which are located at the ligands and the hafnium-oxo core, respectively. By analyzing the spatial distribution of the HOMO orbital, it is observed that the majority of the orbital is localized around the S atoms of the ligands (Fig. S27 online). This observation indicates that S serves as the key site for photocatalytic reduction, exhibiting the highest charge transfer efficiency among all ligands. Furthermore, through the examination of the

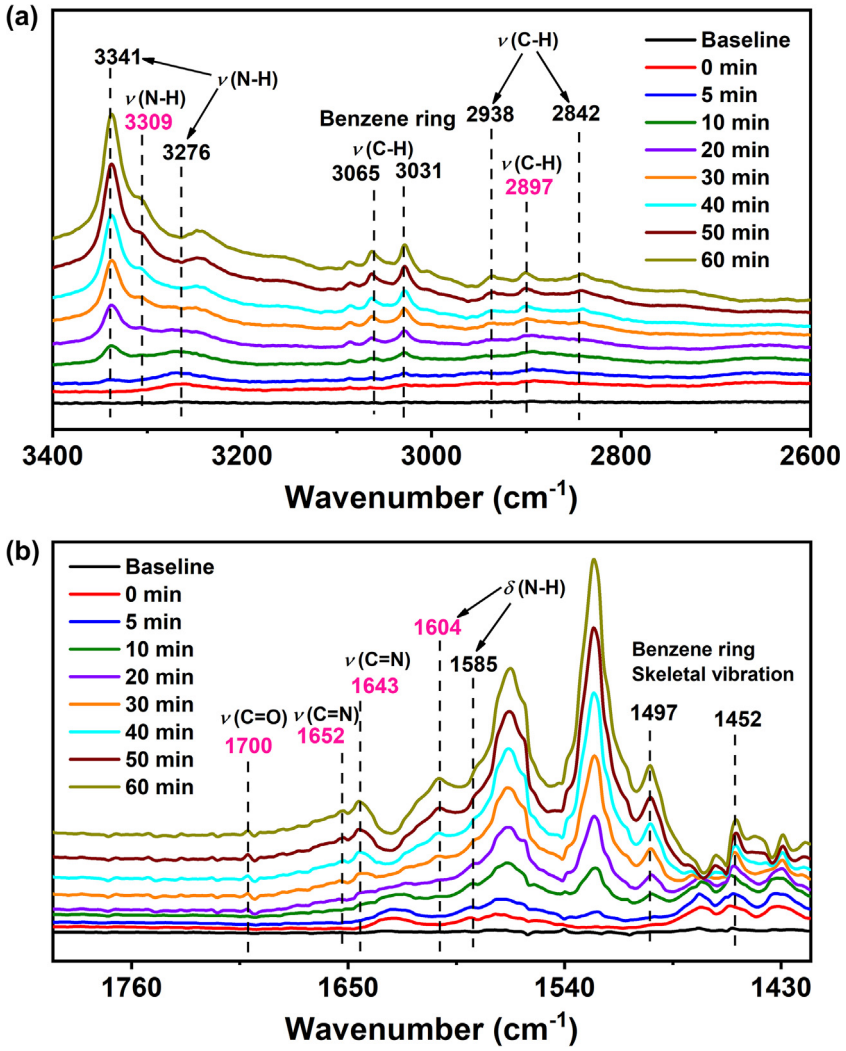

Fig. 4. (Color online) *In-situ* DRIFTS on cluster complexes under dark and irradiation conditions using BA as the reactants. (a) The *in-situ* FTIR spectra from 3400 to 2600 cm^{-1}. (b) The *in-situ* FTIR spectra from 1800 to 1415 cm^{-1}.

potential energy landscape of **Hf_9-TC4A** (highlighted in the red region of Fig. 5b, details in Supplementary materials online), it was discovered that S provides more favorable adsorption sites for nitrogen. Hence, S acts as both an adsorption site for photocatalytic reactants and a facilitator for charge transfer in the photocatalytic reaction, solidifying its significance as the reaction site. Correspondingly, experimental evidence demonstrates a decline in photocatalytic activity when oxygen is used to saturate the S atom, i.e., in the synthesis of **Hf_9-SO_4**. Additionally, our potential energy landscape analysis in Fig. 5b reveals a sharp decrease in the adsorption capability towards nitrogen upon S saturation. This result further substantiates the crucial role of S in photocatalysis.

Therefore, according to the previously reported literature and the above results of the experiment and DFT calculations, the main pathway of photocatalytic oxidative amine coupling reaction of BA can be proposed [46–50]. As depicted in Fig. 5c, firstly, upon irradiation, the **$TC4A^{4-}$** are excited to form photogenerated electron–hole pairs, and the photogenerated electron transfers to the Hf/Zr-oxo core. Then, the locked BA molecules are deprotonated to a cationic amine radical ($PhCH_2NH_2^+$) by photogenerated holes and the O_2 molecules are reduced to form active species $O_2^{\cdot-}$. Subsequently, $PhCH_2NH_2^+$ cation free-radicals and $O_2^{\cdot-}$ are transformed into unstable intermediate species (Ph–CH=NH) and release H_2O_2. Finally, Ph–CH=NH can be converted to target products by two pathways (Fig. 5c). In the first pathway, Ph–CH=NH is attacked by a wandering BA molecule to undergo a nucleophilic addition reaction to produce the coupling product and release ammonia. In the second pathway, Ph–CH=NH rapidly hydrolyzes and releases ammonia gas to generate benzaldehyde, which then undergoes an aldehyde amine condensation reaction with another BA molecule to generate a coupled imine product.

The above results encourage us to investigate whether our strategy has a positive effect on the catalytic performance in other amine oxidation reactions. The oxidation of aromatic amines to achieve aromatic azo compounds with the N=N motif, which are widely used in the synthesis of dyes, medicine, and food additives, plays an increasingly important role in modern industry [51]. However, the challenge of this reaction lies in controlling the selectivity of oxidation products such as azoxybenzene (AOB), azobenzene (AB), and nitrosobenzene (NSB). Inspired by the excellent oxidative capacity of **Hf_9-TC4A** and **Zr_9-TC4A**, they may be potential catalysts in the oxidation reaction of aromatic amines. Based on this awareness, phenylamine was first selected as a model substrate to explore the application of **Hf_9-TC4A** and **Zr_9-TC4A** in the aniline oxidation reaction. After systematic optimization, by employing 10 mg of **Hf_9-TC4A** (or **Zr_9-TC4A**) and 0.1 mmol of phenylamine in 1 mL of methanol with the addition of 60 μL of H_2O_2 at room temperature for 24 h, the formation of AOB as a major product with a conversion of nearly 100% and selectivity of over 90% (Fig. 6a and Figs. S28, S29 online) was achieved. The

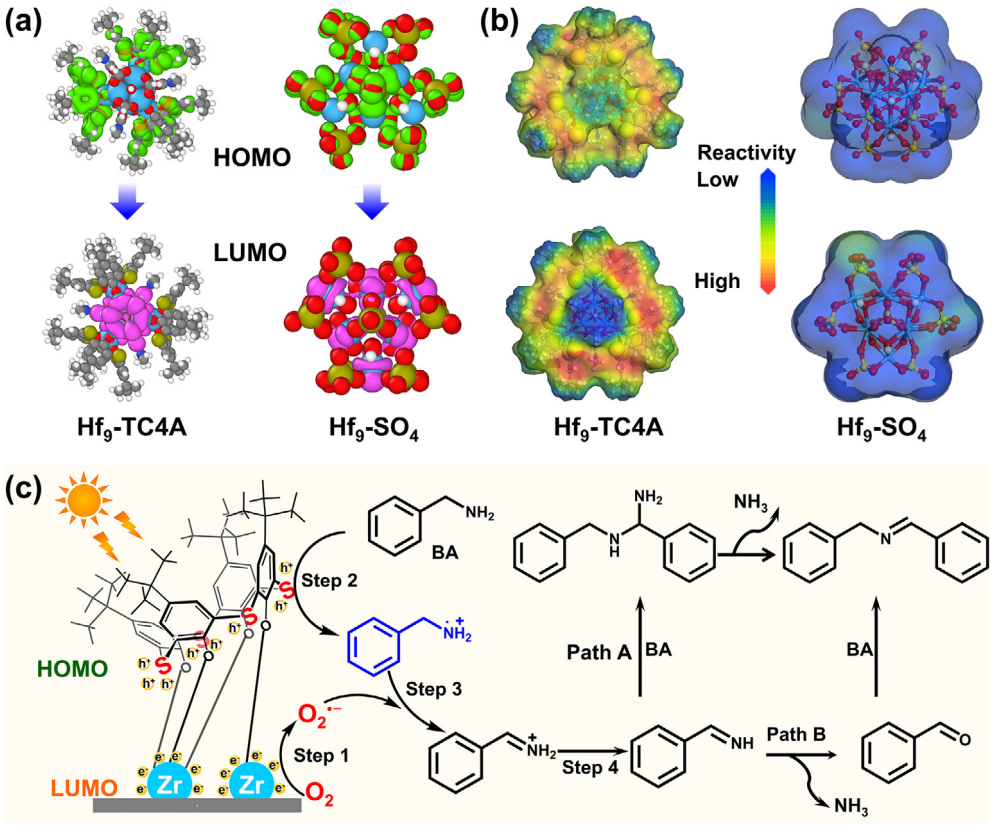

Fig. 5. (Color online) Density functional theory (DFT) calculations and reaction mechanisms. (a) DFT simulates the HOMO and LUMO of **Hf_9-TC4A** and **Hf_9-SO_4**. (b) The potential energy surface (PES) scan. (c) Proposed reaction mechanisms for photocatalytic benzylamine oxidative coupling reaction.

cycling experiment shows that the catalytic activity of **Hf_9-TC4A** decreased very little after five cycles (Fig. 6b), proving the excellent stability of **Hf_9-TC4A** during the catalysis process. To further explore the stability of catalysts, the PXRD and FTIR tests were carried out. Compared with the as-synthesized **Hf_9-TC4A** and **Zr_9-TC4A**, there was no noticeable alteration in the PXRD patterns and IR spectrum of the recovered catalysts (Figs. S30–S33 online), which confirms the structural integrity and stability of **Hf_9-TC4A** and **Zr_9-TC4A** during the photocatalytic reaction.

Some comparative experiments were also carried out to verify the active sites of the catalysts and the necessary conditions for the reaction. As displayed in Fig. 6a, when the ligand **H_4TC4A** was used as the catalyst for the phenylamine oxidation reaction, only trace oxidation products were obtained. In contrast, when the clusters **Hf_9-SO_4** and **Zr_9-SO_4** were employed as catalysts, respectively, the target products with the conversion of 47% (**Hf_9-SO_4**) and 51% (**Zr_9-SO_4**) could be achieved, which suggests that the catalytic active centers are Hf_9 and Zr_9 clusters in **Hf_9-TC4A** and **Zr_9-TC4A**, respectively. Besides, as shown in Table S4 (entry 2, 3, online), both catalysts and H_2O_2 are indispensable for aniline oxidation reaction in the catalytic system, otherwise, only trace quantities of target products can be obtained. Moreover, the poor performance of the physical mixture indicates that the coordination between ligands and metals is crucial for the catalytic performance of the catalysts (Fig. S34 online).

By experiment, the mechanism of aniline oxidation in our catalytic system can be revealed. As proposed by previous works, the oxidation of aniline is reported to proceed through two generally believed mechanisms: a radical mechanism (Scheme S1 online) and the nitrosobenzene intermediate mechanism (Scheme S2 online) [52]. A quenching experiment was carried out to identify the real reaction mechanism. When 2,6-di-*tert*-butyl-4-methylphenol (BHT) as the radical scavenger was added to the reaction mixture, the reaction proceeded normally, indicating that the radical reaction mechanism is not the main process occurring in this system (Scheme S3 and Table S4, entry 4, online). Besides, the detected trace quantities of NSB during the reaction process further demonstrate that the reaction mechanism in our catalytic system complied with the nitrosobenzene intermediate mechanism.

DFT calculations were conducted to provide further insight into the detailed reaction processes. Firstly, we focused on the adsorption of aniline and H_2O_2. Based on the previous findings from the potential energy surface (PES) scan, which explored the energy of the nitrogen atom at different positions on the complexes' surface, it was observed that aniline preferentially adsorbs onto S sites. In addition, for the adsorption of H_2O_2, as the adsorbate is oxygen (O), direct utilization of the potential energy surface search results is not feasible. Therefore, we directly calculated the adsorption energy on Hf and S atoms. Fig. 6c illustrates that the adsorption energy of H_2O_2 is lower on Hf sites (2.707 eV) compared to S atoms (2.269 eV), indicating that the primary adsorption sites for H_2O_2 are on Hf sites. After the adsorption of aniline and H_2O_2, they react to form Ph-NHOH. According to the comparison of calculated energies, Ph-NHOH preferentially adsorbs onto Hf rather than S sites (Fig. 6c, d and Fig. S35 online). Hence, subsequent reactions are expected to take place on the Hf sites. Therefore, the mechanism of aniline oxidation on hafnium clusters can be proposed. Aniline molecules are adsorbed on naked S atoms of ligands and H_2O_2 is adsorbed on the Hf sites and activated to produce HOO·, which is the active species for this reaction. Subsequently, aniline is attacked by HOO· to generate Ph-NHOH (Fig. 6e, step 1), which was readily oxidized to NSB (Fig. 6e, step 2). Then AOB, a more inclined product was formed by the condensation reaction

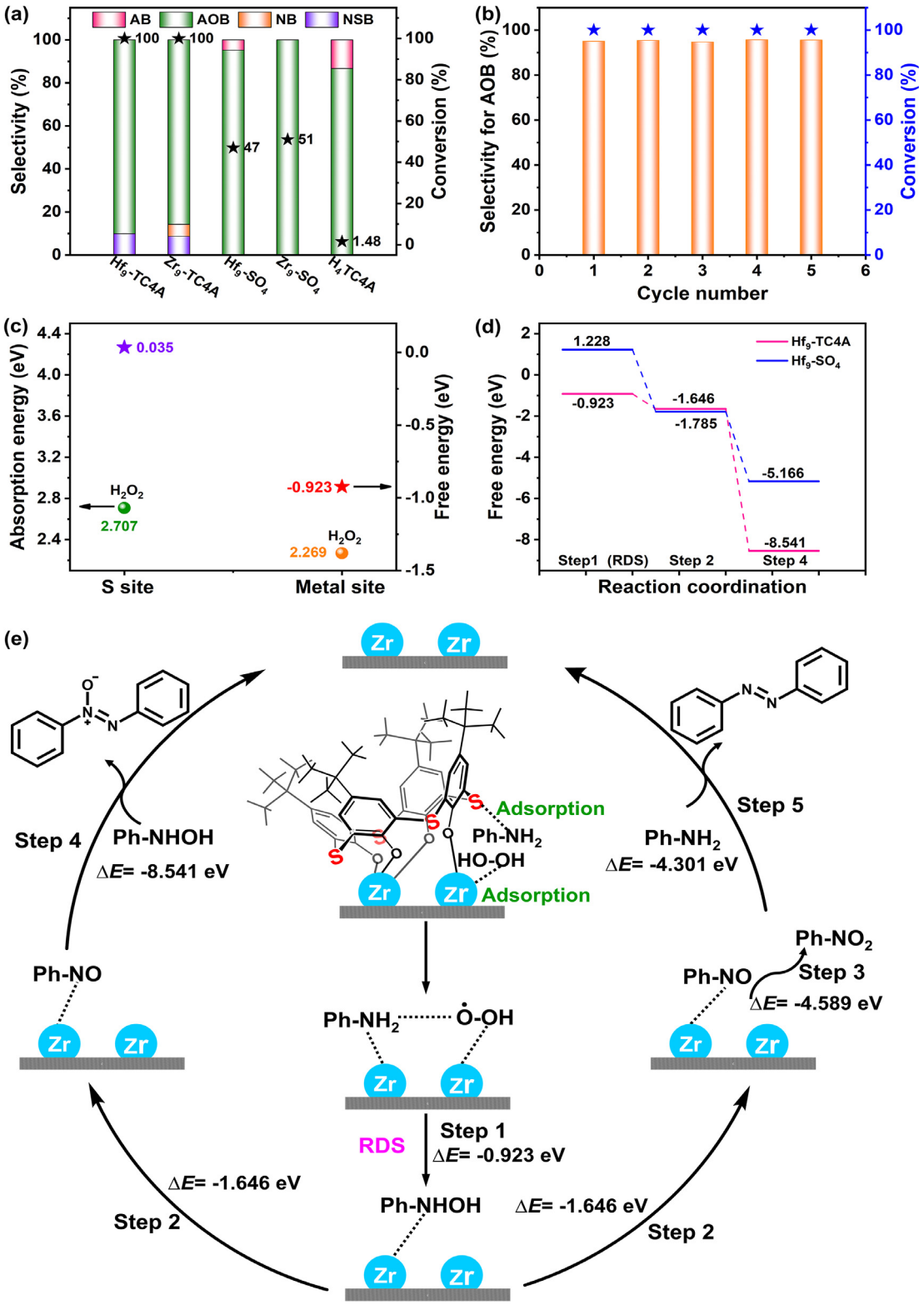

Fig. 6. (Color online) The performance of the oxidation reaction of phenylamine and the corresponding theoretical calculations. (a) Selective oxidation of anilines to azoxybenzenes, azobenzenes, and nitrosobenzenes with peroxide as the oxidant. (b) Conversion and selectivity of oxidative of aniline with **Hf_9-TC4A** in five repeating cycles. (c) The adsorption energy of H_2O_2 and the free energy of the formation of the intermediate (Ph-NHOH) in RDS on the S site and the metal site. (d) Free energy diagram (FED) of **Hf_9-TC4A** and **Hf_9-SO_4** for aniline oxidation to produce AOB. (e) Proposed reaction mechanism for the aniline oxidation reaction and reaction energy change of each step after adsorption at the Hf site.

between NSB and Ph-NHOH (Fig. 6c, step 4) since the reaction energy of step 4 is lower than that of step 3 and step 5. Additionally, we discovered that the bond formation between aniline and H_2O_2 in step 1 exhibits the most favorable reaction energy (−0.923 eV) among all the steps, serving as the rate-determining step (RDS) for the entire process. This finding holds true for **Hf_9-SO_4** as well. By comparing the reaction energies of the RDS for both **Hf_9-TC_4A** and **Hf_9-SO_4** (Fig. 6d and Figs. S35, S36 online), it is evi-

dent that **Hf_9-TC4A** exhibits a lower RDS energy, further emphasizing the significance of naked S atoms in the reaction.

To investigate the general applicability of the reaction, the substrate scope was expanded. As shown in Table S5 (online), for the photocatalytic oxidative coupling reaction of BA, benzylamines with different electron-donating or electron-withdrawing groups (such as Me-, MeO-, F-, Cl- and Br-) can be converted into target products with satisfactory conversions, following the order of electron-donating groups > electron-withdrawing groups. This result indicates that the electronic effect plays a role in the BA oxidation reaction [53]. Moreover, this effect is more pronounced in the aniline oxidation reaction. As presented in Table S6 (online), the substrates with an electron-donating group (*p*-Me-, *m*-Me-, and *o*-Me-) are better conversion than those with the electron-withdrawing group (Cl- and Br-). Besides, the effect of steric hindrance on the reaction was also explored in the aniline oxidation reaction. The results show that there is no significant difference between the yields of *p*-, *m*-, and *o*-substituted products (Table S6 online), which means that the steric hindrance has no obvious effect in our catalytic system.

4. Conclusion

To sum up, for the first time, we synthesized two Zr/Hf-based clusters modified with 4-*tert*-butylthiacalix[4]arene ligands (**Zr_9-TC4A** and **Hf_9-TC4A**) and used them as catalysts for photo-induced oxidative coupling of benzylamine reaction and aniline oxidation reaction in H_2O_2 system. Thanks to the modification of 4-*tert*-butylthiacalix[4]arene, both light absorption and electron transfer capabilities of Zr/Hf-based clusters have been greatly enhanced, which allows them to exhibit excellent catalytic performance with a high substrate conversion (>99%) and product selectivity (>90%) in these two types of amine oxidation reaction. The DFT calculations prove that the bare S atoms embedded in ligands can synergize with the metal to complete the catalytic process in two ways: (i) unsaturated S atoms act as active sites in synergy with metal active sites for catalysis, and (ii) unsaturated S atoms as adsorption sites for reaction substrate in concert with metal active sites to complete the catalytic reaction. This work pioneered the application of Zr/Hf-based cluster complexes in photocatalytic reactions and, more importantly, it proposed the synergistic catalysis of naked S atoms in amine oxidation reactions for the first time.

Conflict of interest

The authors declare that they have no conflict of interest.

Acknowledgments

This work was supported by the National Natural Science Foundation of China (22225109, 92061101, 22071109, and 22101089), the Top Youth Project of Guangdong Province Pearl River Talents Program (2021QN02L617), the Excellent Youth Foundation of Jiangsu Province Natural Science Foundation (BK20211593), the Open Fund of Energy and Materials Chemistry Joint Laboratory of South China Normal University and Guangzhou Tinci Materials Technology (SCNU-TINCI-202204), and Guangdong Province Basic and Applied Basic Research Foundation (2023A1515030097 and 2020A1515110836).

Author contributions

Sheng-Nan Sun, Jiang Liu, and Ya-Qian Lan conceived and designed the idea. Sheng-Nan Sun and Li-Ling He synthesized the compounds. Sheng-Nan Sun and Qian Niu designed and conducted characterizations and related electrocatalysis experiments. Sheng-Nan Sun and Jing-Wen Shi assisted with the characterizations and collected the data. Sheng-Nan Sun, Jiao-Min Lin, Qing Huang, Jiang Liu, and Ya-Qian Lan discussed the results and prepared the manuscript. All the authors reviewed and contributed to this paper.

Appendix A. Supplementary materials

Supplementary materials to this article can be found online at https://doi.org/10.1016/j.scib.2023.11.047.

References

[1] Ni D, Cheng Y, Zhang J, et al. Advances in ultra-high temperature ceramics, composites, and coatings. J Adv Ceram 2022;11:1–56.
[2] Wei Z-Y, Meng G-H, Chen L, et al. Progress in ceramic materials and structure design toward advanced thermal barrier coatings. J Adv Ceram 2022;11:985–1068.
[3] Sheikh S, Shafeie S, Hu Q, et al. Alloy design for intrinsically ductile refractory high-entropy alloys. J Appl Phys 2016;120:164902.
[4] Du C, Yuan H, Zhu X, et al. Fabrication of antibacterial Zr-BMG biomimetic surfaces by femtosecond laser. Surf Interfaces 2023;37:102740.
[5] Li X, Liu J, Lv R, et al. Novel carbon-coated zirconium oxide nanocomposites enable ultrahigh oxidant utilization efficiency for selective degradation of organic contaminants. Chem Eng J 2023;463:142369.
[6] Zhang Y, de Azambuja F, Parac-Vogt TN. The forgotten chemistry of group(IV) metals: a survey on the synthesis, structure, and properties of discrete Zr(IV), Hf(IV), and Ti(IV) oxo clusters. Coord Chem Rev 2021;438:213886.
[7] Van den Eynden D, Pokratath R, De Roo J. Nonaqueous chemistry of group 4 oxo clusters and colloidal metal oxide nanocrystals. Chem Rev 2022;122:10538–72.
[8] Zhao C, Han Y-Z, Dai S, et al. Microporous cyclic titanium-oxo clusters with labile surface ligands. Angew Chem Int Edit 2017;56:16252–6.
[9] Yuan S, Qin J-S, Su J, et al. Sequential transformation of zirconium(IV)-MOFs into heterobimetallic MOFs bearing magnetic anisotropic cobalt(II) centers. Angew Chem Int Edit 2018;57:12578–83.
[10] Lin X-C, Wang Y-M, Chen X, et al. A photosensitizing metal–organic framework as a tandem rreaction catalyst for primary alcohols from terminal alkenes and alkynes. Angew Chem Int Edit 2023;62:e202306497.
[11] Sun K, Qian Y, Jiang H-L. Metal-organic frameworks for photocatalytic water splitting and CO_2 reduction. Angew Chem Int Edit 2023;62:e202217565.
[12] Li N, Liu J, Liu J-J, et al. Self-assembly of a phosphate-centered polyoxo-titanium cluster: discovery of the heteroatom keggin family. Angew Chem Int Edit 2019;58:17260–4.
[13] Fang W-H, Zhang L, Zhang J. Synthetic strategies, diverse structures and tuneable properties of polyoxo-titanium clusters. Chem Soc Rev 2018;47:404–21.
[14] Vigolo M, Borsacchi S, Sorarù A, et al. Engineering of oxoclusters-reinforced polymeric materials with application as heterogeneous oxydesulfurization catalysts. Appl Catal B: Environ 2016;182:636–44.
[15] Faccioli F, Bauer M, Pedron D, et al. Hydrolytic stability and hydrogen peroxide activation of zirconium-based oxoclusters. Eur J Inorg Chem 2015;2015:210–25.
[16] Song Y, Li Z, Zhu Y, et al. Titanium hydroxide secondary building units in metal–organic frameworks catalyze hydrogen evolution under visible light. J Am Chem Soc 2019;141:12219–23.
[17] Cadiau A, Kolobov N, Srinivasan S, et al. A titanium metal–organic framework with visible-light-responsive photocatalytic activity. Angew Chem Int Edit 2020;59:13468–72.
[18] Ousaka N, Itakura M, Nagasaka A, et al. Water-mediated reversible control of three-state double-stranded titanium(IV) helicates. J Am Chem Soc 2021;143:4346–58.
[19] Rojas-Buzo S, Bohigues B, Lopes CW, et al. Tailoring Lewis/Brønsted acid properties of MOF nodes via hydrothermal and solvothermal synthesis: simple approach with exceptional catalytic implications. Chem Sci 2021;12:10106–15.
[20] Lu Z, Liu J, Zhang X, et al. Node-accessible zirconium MOFs. J Am Chem Soc 2020;142:21110–21.
[21] Li J, Huang J-Y, Meng Y-X, et al. Zr- and Ti-based metal–organic frameworks: synthesis, structures and catalytic applications. Chem Commun 2023;59:2541–59.
[22] Jerozal RT, Pitt TA, MacMillan SN, et al. High-concentration self-assembly of zirconium- and hafnium-based metal–organic materials. J Am Chem Soc 2023;145:13273–83.
[23] Zhao Y, Qi S, Niu Z, et al. Robust corrole-based metal–organic frameworks with rare 9-connected Zr/Hf-oxo clusters. J Am Chem Soc 2019;141:14443–50.
[24] Mian MR, Wang X, Wang X, et al. Structure–activity relationship insights for organophosphonate hydrolysis at Ti(IV) active sites in metal–organic frameworks. J Am Chem Soc 2023;145:7435–45.

[25] Jiang H, Zhang W, Kang X, et al. Topology-based functionalization of robust chiral Zr-based metal–organic frameworks for catalytic enantioselective hydrogenation. J Am Chem Soc 2020;142:9642–52.
[26] Liu J-J, Li N, Sun J-W, et al. Ferrocene-functionalized polyoxo-titanium cluster for CO_2 photoreduction. ACS Catal 2021;11:4510–9.
[27] Xie W-L, Li X-M, Lin J-M, et al. Keeping superprotonic conductivity over a wide temperature region via sulfate hopping sites-decorated zirconium-oxo clusters. Small 2022;18:2205444.
[28] Shi J-W, Sun S-N, Liu J, et al. Calixarene-functionalized stable bismuth oxygen clusters for specific CO_2-to-HCOOH Electroreduction. ACS Catal 2022;12:14436–44.
[29] Lai Q-s, Li X-X, Zheng S-T. All-inorganic POM cages and their assembly: a review. Coordin Chem Rev 2023;482:215077.
[30] Zhang L, Li X-X, Lang Z-L, et al. Enhanced cuprophilic interactions in crystalline catalysts facilitate the highly selective electroreduction of CO_2 to CH_4. J Am Chem Soc 2021;143:3808–16.
[31] Lin J, Li N, Yang S, et al. Self-assembly of giant Mo_{240} hollow opening dodecahedra. J Am Chem Soc 2020;142:13982–8.
[32] Ge R, Li X-X, Zheng S-T. Recent advances in polyoxometalate-templated high-nuclear silver clusters. Coord Chem Rev 2021;435:213787.
[33] Wang X, Xie H, Knapp JG, et al. Mechanistic investigation of enhanced catalytic selectivity toward alcohol oxidation with Ce oxysulfate clusters. J Am Chem Soc 2022;144:12092–101.
[34] Deng G, Malola S, Yuan P, et al. Enhanced surface ligands reactivity of metal clusters by bulky ligands for controlling optical and chiral properties. Angew Chem Int Edit 2021;60:12897–903.
[35] Shen H, Xu Z, Hazer MSA, et al. Surface coordination of multiple ligands endows n-heterocyclic carbene-stabilized gold nanoclusters with high robustness and surface reactivity. Angew Chem Int Edit 2021;60:3752–8.
[36] Zhu M, Yao Q, Liu Z, et al. Surface engineering assisted size and structure modulation of gold nanoclusters by ionic liquid cations. Angew Chem Int Edit 2022;61:e202115647.
[37] Guan Z-J, Zeng J-L, Nan Z-A, et al. Thiacalix[4]arene: new protection for metal nanoclusters. Sci Adv 2016;2:e1600323.
[38] Guan Z-J, Hu F, Yuan S-F, et al. The stability enhancement factor beyond eight-electron shell closure in thiacalix[4]arene-protected silver clusters. Chem Sci 2019;10:3360–5.
[39] He C, Zou Y-H, Si D-H, et al. A porous metal-organic cage liquid for sustainable CO_2 conversion reactions. Nat Commun 2023;14:3317.
[40] Wang Z, Alkan F, Aikens CM, et al. An ultrastable 155-nuclei silver nanocluster protected by thiacalix[4]arene and cyclohexanethiol for photothermal conversion. Angew Chem Int Edit 2022;61:e202206742.
[41] Zhang C, Wang Z, Si W-D, et al. Solvent-induced isomeric Cu_{13} nanoclusters: chlorine to copper charge transfer boosting molecular oxygen activation in sulfide selective oxidation. ACS Nano 2022;16:9598–607.
[42] Wang Z, Li L, Feng L, et al. Solvent-controlled condensation of $[Mo_2O_5(PTC4A)_2]^{6-}$ metalloligand in stepwise assembly of hexagonal and rectangular Ag_{18} nanoclusters. Angew Chem Int Edit 2022;61:e202200823.
[43] Yang X-X, Yu W-D, Yi X-Y, et al. Monocarboxylate-driven structural growth in Calix[n]arene-polyoxotitanate hybrid systems: utility in hydrogen production from water. Chem Commun 2020;56:14035–8.
[44] Li N, Liu J-J, Sun J-W, et al. Calix[8]arene-constructed stable polyoxo-titanium clusters for efficient CO_2 photoreduction. Green Chem 2020;22:5325–32.
[45] Wang X, Yu Y, Wang Z, et al. Thiacalix[4]arene-protected titanium–oxo clusters: influence of ligand conformation and Ti–S coordination on the visible-light photocatalytic hydrogen production. Inorg Chem 2020;59:7150–7.
[46] Xu C, Liu H, Li D, et al. Direct evidence of charge separation in a metal–organic framework: efficient and selective photocatalytic oxidative coupling of amines via charge and energy transfer. Chem Sci 2018;9:3152–8.
[47] Zhao F-J, Zhang G, Ju Z, et al. The combination of charge and energy transfer processes in MOFs for efficient photocatalytic oxidative coupling of amines. Inorg Chem 2020;59:3297–303.
[48] Hou T, Gao Z, Zhang J, et al. Simultaneously enhanced activity and selectivity for $C(sp_3)$–H bond oxidation under visible light by nitrogen doping. Trans Tianjin Univ 2021;27:331–7.
[49] Liu W, Wang Y, Huang H, et al. Spatial decoupling of redox chemistry for efficient and highly selective amine photoconversion to imines. J Am Chem Soc 2023;145:7181–9.
[50] Chen H, Liu C, Guo W, et al. Functionalized UiO-66(Ce) for photocatalytic organic transformation: the role of active sites modulated by ligand functionalization. Catal Sci Technol 2022;12:1812–23.
[51] Dai Y, Xiong Y. Control of selectivity in organic synthesis via heterogeneous photocatalysis under visible light. Nano Res Energy 2022;1:9120006.
[52] Qin J, Long Y, Sun F, et al. $Zr(OH)_4$-catalyzed controllable selective oxidation of anilines to azoxybenzenes, azobenzenes and nitrosobenzenes. Angew Chem Int Edit 2021;10:8717–26.
[53] Li S, Li L, Li Y, et al. Fully conjugated donor–acceptor covalent organic frameworks for photocatalytic oxidative amine coupling and thioamide cyclization. ACS Catal 2020;10:8717–26.

Sheng-Nan Sun received her Bachelor's degree (2017) from Jiangsu University of Science and Technology and her M.S. degree from Nanjing Normal University (2020). Now, she is a Ph.D. candidate at South China Normal University. Her current research focuses on the synthesis of crystalline complexes as electrocatalysts for the electrocatalytic reduction of carbon dioxide and electrocatalytic organic reaction.

Qian Niu received her Bachelor's degree (2016) from Nanjing Normal University, and she is currently pursuing her Ph.D. degree at Nanjing Normal University. Her current research focuses on the structural design synthesis and performance study of thorium clusters.

Jiao-Min Lin received his Ph.D. degree (2015) from Sun Yat-sen University under the supervision of Prof. Jie-Peng Zhang. He then worked as a lecturer at College of Chemistry and Materials Science, Shanghai Normal University. In 2022, he joined Prof. Ya-Qian Lan's group at School of Chemistry, South China Normal University. His current research interest focuses on the syntheses, structures and properties of molecular-based metal cluster.

Jiang Liu obtained his Ph.D. degree from Sun Yat-sen University under the supervision of Prof. Ming-Liang Tong. In 2022, he joined South China Normal University and became a professor of Chemistry. His research interest focuses on the development of functional crystalline materials (e.g., metal–organic clusters/frameworks) applied for the photo-/electro-catalytic conversion of inorganic/organic small molecule to valued-added products.

Ya-Qian Lan received his B.S. and Ph.D. degrees (2009) from Northeast Normal University, under the supervision of Prof. Zhong-Min Su. In 2010, he joined the National Institute of Advanced Industrial Science and Technology (AIST, Japan) working as a JSPS postdoctoral fellow. In 2012, he became a professor of Chemistry at Nanjing Normal University. He joined South China Normal University in 2021, and is now a professor of Chemistry. His current research interest focuses on the synthesis of new crystalline materials and catalytic research related to clean energy applications.